



Diagnosis and monitoring denosumab therapy of giant cell tumors of bone: radiologic-pathologic correlation

Maryse Lejoly^{1,2} · Thomas Van Den Berghe^{1,2} · David Creybens^{2,3} · Wouter Huysse¹ · Lore Lapeire⁴ · Gwen Sys⁵ · Koenraad Verstraete^{1,2}

Received: 24 May 2023 / Revised: 10 July 2023 / Accepted: 10 July 2023 / Published online: 29 July 2023
© The Author(s), under exclusive licence to International Skeletal Society (ISS) 2023

Abstract

Objective To determine the value of CT and dynamic contrast-enhanced (DCE-)MRI for monitoring denosumab therapy of giant cell tumors of bone (GCTB) by correlating it to histopathology.

Materials and methods Patients with GCTB under denosumab treatment and monitored with CT and (DCE-)MRI (2012–2021) were retrospectively included. Imaging and (semi-)quantitative measurements were used to assess response/relapse. Tissue samples were analyzed using computerized segmentation for vascularization and number of neoplastic and giant cells. Pearson's correlation/Spearman's rank coefficient and Kruskal-Wallis tests were used to assess correlations between histopathology and radiology.

Results Six patients (28 ± 8 years; five men) were evaluated. On CT, good responders showed progressive re-ossification ($+7.8$ HU/month) and cortical remodeling (woven bone). MRI showed an SI decrease relative to muscle on T1-weighted (-0.01 A.U./month) and on fat-saturated T2-weighted sequences (-0.03 A.U./month). Time-intensity-curves evolved from a type IV with high first pass, high amplitude, and steep wash-out to a slow type II. An increase in time-to-peak ($+100\%$) and a decrease in K_{trans} (-71%) were observed. This is consistent with microscopic examination, showing a decrease of giant cells (-76%), neoplastic cells (-63%), and blood vessels (-28%). There was a strong statistical significant inverse correlation between time-to-peak and microvessel density ($\rho = -0.9$, $p = 0.01$). Significantly less neoplastic ($p = 0.03$) and giant cells ($p = 0.04$) were found with a time-intensity curve type II, compared to a type IV. Two patients showed relapse after initial good response when stopping denosumab. Inverse imaging and pathological findings were observed.

Conclusion CT and (DCE-)MRI show a good correlation with pathology and allow adequate evaluation of response to denosumab and detection of therapy failure.

Keywords Giant cell tumor of bone · Denosumab · (DCE-)MRI · Histopathology · Vascularization · Correlation · K_{trans} · Time-to-peak · CT · Microvessel density

✉ Maryse Lejoly
maryse.lejoly@gmail.com

¹ Department of Radiology and Medical Imaging, Ghent University Hospital, 1K12/Entrance 12 Route 1590, Corneel Heymanslaan 10, B-9000 Ghent, Belgium

² Department of Diagnostic Sciences, Ghent University, Ghent, Belgium

³ Department of Pathology, Ghent University Hospital, Ghent, Belgium

⁴ Department of Medical Oncology, Ghent University Hospital, Ghent University, Ghent, Belgium

⁵ Department of Orthopedics and Traumatology, Ghent University Hospital, Ghent University, Ghent, Belgium

Introduction

Giant cell tumor of bone (GCTB) is characterized by neoplastic proliferating mononuclear stromal cells (NC) and osteoclast-like giant cells (GC). The NCs express receptor activator of nuclear factor kappa-B-ligand (RANKL), which binds to RANK on the GCs and endothelial cells, inducing cell activation and neovascularization, leading to bone resorption. A total of 96% of GCTB have a driver mutation of glycine 34 in H3F3A in the NC which is useful for the (differential) diagnosis. Despite the benign character, GCTB can be locally aggressive and can metastasize in 5.1% [1–4].

GCTB predominantly occurs between 20 and 45 years, without clear sex preference. It accounts for 20% of benign

bone tumors [2, 3]. A total of 70% of GCTB are located in the epiphysis of long bones and 25% in flat bones [2, 3]. The epiphyseal location leads to joint dysfunction and sometimes pathological fractures. Mechanical and activity-dependent pain are the most prominent symptoms [3, 5].

The treatment of choice is curettage with or without local adjuvant or resection. Local recurrence is seen in 15–50%, with a higher risk after curettage without local adjuvants [1, 2]. Denosumab was introduced to treat skeletally mature patients with inoperable GCTB [5, 6]. It is a fully humanized monoclonal antibody targeting RANKL, inhibiting GC and endothelial activation and inducing apoptosis. Histologically, response to denosumab is defined as >90% decrease of GCs [5, 7]. Clinical and histological improvement is observed by symptom decrease, woven bone formation, and calcification with rim formation. Due to the interaction between GCs and NCs, a reduction of NCs is also observed. However, they continue to proliferate at a slower pace [1, 5, 6, 8].

Because of the high recurrence risk, a good follow-up schedule when interrupting treatment is necessary [9–11]. While imaging plays a crucial role in the diagnosis and follow-up of GCTB, objective studies on lesion evolution and pathological correlation are missing. Conventional radiographs display all features for GCTB diagnosis. In follow-up and operative planning, CT assesses cortical thinning,

pathologic fractures, and fracture consolidation, while MRI evaluates soft tissue invasion. Dynamic contrast-enhanced (DCE-)MRI evaluates tumoral microcirculation in a non-invasive way (vessel density, vascular permeability, perfusion, extravascular space, and interstitial volume) [12]. Figure 1 illustrates the functioning of GCTB and the effect of denosumab on bone and blood vessels [13–16].

This proof-of-concept study on six patients aims to describe the effects of denosumab on imaging and pathological findings and evaluates the value of CT and (DCE-)MRI for follow-up during treatment in good and poor responders, with pathological correlation.

Methods

Patient population

Institutional review board approval (BC-11285) and informed consent were obtained. Patients with GCTB under denosumab treatment (2012–2021, Ghent University Hospital) were retrospectively included. Exclusion criteria for initially eligible patients were absence of histopathology and (DCE-)MRI examination more than 6 months before biopsy/curettage (Figure 2). Diagnosis was histologically confirmed by a pathologist with 15 years of experience in

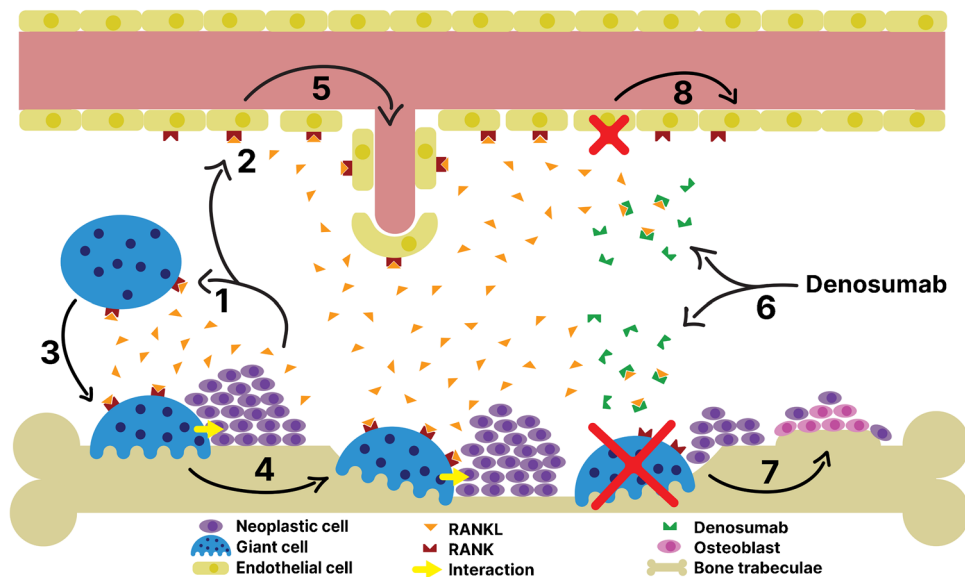


Fig. 1 Functioning of a giant cell tumor of bone and the effect of denosumab therapy. The neoplastic cells of the giant cell tumor of bone express receptor activator of nuclear factor kappa-B ligand (RANKL), which will bind to receptor activator of nuclear factor kappa-B (RANK) on giant cells (1) and on endothelial cells (2). This binding of the RANKL on RANK will activate giant cells (3) leading to bone resorption (4). The binding of RANKL to RANK on endothelial cells will lead to neovascularization and increased permeability

of blood vessels (5). However, when patients receive denosumab, the RANKL will bind to denosumab instead of RANK on giant cells and endothelial cells (6). Giant cells will go through apoptosis and osteoblasts will start proliferating (7), leading to new woven bone formation. Stimulated endothelial cells, which are no longer stimulated by the binding of RANKL to RANK, will go through apoptosis as well, leading to disappearance of neovascularization and decrease of vessel permeability (8)

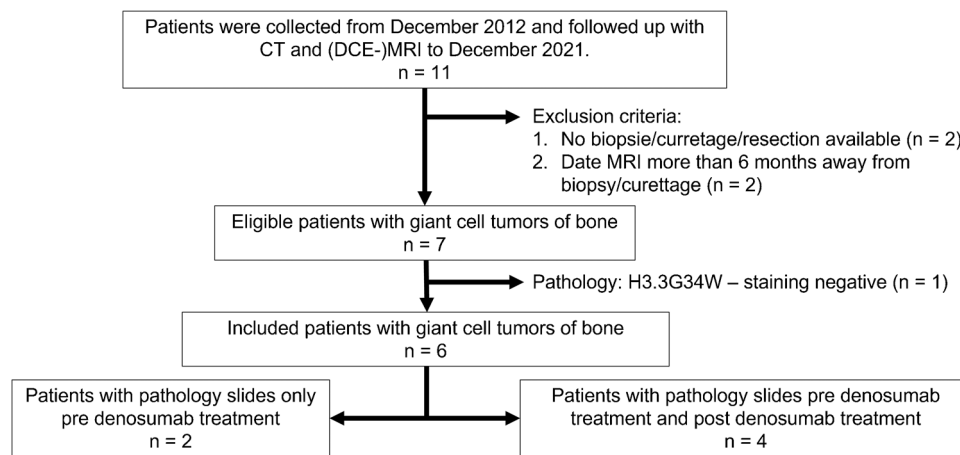


Fig. 2 Flowchart with patient collection, exclusion criteria, and included patients. Apart from the initially introduced exclusion criteria, one initially eligible patient was excluded because the H3.3G34W staining, which is very sensitive and specific for giant cell tumors of bone, turned out to be negative reflecting that this patient did not represent the classical giant cell tumor of bone. All six included patients

had a DCE-MRI pre-denosumab and post-denosumab treatment and four patients had pathology samples before and after denosumab treatment. Two patients only had pathology samples of the pre-denosumab treatment initial diagnostic biopsy but did not undergo curettage post-denosumab treatment yet. *DCE-MRI* = dynamic contrast-enhanced MRI; *n* = number

bone tumors (D.C.). Finally, six patients were included. All patients had a biopsy before denosumab treatment and four patients also had a curettage after denosumab treatment, providing histopathological slides for correlation with radiology. All patients received follow-up with CT and (DCE-)MRI, alternating, six-monthly. One CT and one (DCE-)MRI (closest to biopsy/curettage) were analyzed before and after denosumab treatment for all patients. Imaging and pathology samples were in average $2 (\pm 2)$ months away from each other. Two patients had a late curettage after denosumab treatment and showed recurrence; in these patients, a third (DCE-)MRI was also analyzed after denosumab treatment, before recurrence occurred.

CT imaging

CT was performed using Somatom Definition Flash (Siemens, Erlangen, Germany). Slice thickness varied from 1 to 3 mm. Largest diameter in three orthogonal directions was measured. In addition, the mean Hounsfield unit (HU) and the surface area of the giant cell tumor of bone were calculated on all slices. Volume (Eq. 1) and surface-weighted average HU (Eq. 2) were calculated to follow up over time. The changes were correlated with changes on the histopathological samples.

$$V = \sum_{i=1}^n \text{surface area } (i) \cdot \text{slice thickness} \quad (1)$$

(*V* = tumor volume; *n* = number of slices; *i* = slice number *i*)

$$\text{Surface-weighted HUmean} = \frac{\sum_{i=1}^n \text{surface slice } (i) \cdot \text{mean HU slice } (i)}{\sum_{i=1}^n \text{surface slice } (i)} \quad (2)$$

(HU = Hounsfield Unit; *n* = number of slices; *i* = slice number *i*)

MR imaging

1.5T MRI studies were obtained on Magnetom Avanto Fit and Symphony Tim devices (Siemens, Erlangen, Germany). Slice thickness and spacing varied from 2.0 to 6.0 mm and 2.2 to 7.2 mm, respectively. DCE-MRI was performed with a T1-weighted (T1w) 3D Twist-Vibe sequence. Largest diameter in three orthogonal directions was measured on T1w sequences. In addition, mean signal intensity (SI) and surface area were calculated on T1w-saturated and fat-saturated T2w (T2FSw) sequences on all slices to calculate the surface-weighted SI on T1w and T2FSw sequences, to follow up over time (Eq. 3). As a reference, the SI of a fat-free muscle region-of-interest was measured. The same muscle was used between MRI studies in time. Finally, the mean tumoral SI relative to muscle was calculated (Eq. 4).

Both on CT and MRI imaging, all imaging measurements and tumoral segmentations were performed by two pretrained observers (M.L. and T.V.D.B. with 3 and 4 years of experience in bone tumor imaging, respectively) under direct supervision of K.V. (musculoskeletal radiologist with more than 35 years of experience) to increase accuracy. All available CT and MRI sequences were used and correlated

in order to perform pixel-by-pixel detailed manual segmentation of the tumoral borders and to perform detailed measurements. Inter-reader analysis was not performed since all cases of GCTB could be clearly delineated leading to highly consistent measurements by multiple observers, both at diagnosis and during treatment follow-up. For different follow-up CT and MRI studies, the exact same segmentation areas were maintained.

$$\text{Surface-weighted SI mean} = \frac{\sum_{i=1}^n \text{surface slice } (i) \cdot \text{mean SI slice } (i)}{\sum_{i=1}^n \text{surface slice } (i)} \quad (3)$$

(i = slice number; n = number of slices; SI = signal intensity)

$$\text{Rel surface-weighted SI mean} = \frac{\text{surface-weighted SI mean}}{\text{muscle SI mean}} \quad (\text{SI} = \text{signal intensity}) \quad (4)$$

The DCE-MRI was evaluated using SyngoVia VB50 (Siemens, Erlangen, Germany). The region-of-interest captured the entire tumor on the slice with the largest diameter. A second and third region-of-interest was drawn in a reference fat-free region of a muscle and a blood vessel (zone without flow artifacts) to calculate relative parameters and was kept constant between follow-up DCE-MRI studies. First, a qualitative analysis was performed by evaluating the time-intensity curves (TIC), reflecting the exchange of gadolinium contrast agent between the intravascular and interstitial space with characteristic curve types (Figure 3A) [17–19]. Secondly, semi-quantitative analysis was performed by describing the characteristics of the TIC: The wash-in slope, wash-out slope, time-to-peak (TTP), positive enhancement integral, and area-under-the-curve were calculated. Moreover, the K_{trans} (volume transfer constant), V_e (extracellular-extravascular-volume-fraction), and K_{ep} (efflux rate constant) were calculated (modified Tofts model). The area-under-the-curve was calculated from the time-concentration curve [18, 20].

Pathology

The tissue samples were subjected to 4% formalin fixation and paraffin embedding. Bone-rich tissue was decalcified by the use of standard procedures with incubation in EDTA. Subsequently, 4- μm tissue sections were cut and stained with H&E. Immunohistochemistry was performed on 4- μm -thick sections of formalin-fixed, paraffin-embedded material with a Benchmark XT immunostainer (Ventana Medical Systems, Tucson, AZ, USA). Primary monoclonal antibodies were CD34 (1:100; QBE10; Dako, Denmark) and H3.3 G34W (1:800; RM263; RevMab Biosciences, USA). Visualization was achieved with the Ultraview Universal DAB Detection kit (Ventana Medical Systems, Tucson, AZ, USA). Appropriate positive and negative controls were used throughout.

The slide with largest diameter was double-stained with CD34 (function: vascularization; color: red) and Histone 3.3 (H3F3A) G34W (H3.3G34W) (function: NCs; color: brown) and scanned using the Nanozoomer 2.0-RS (Hamamatsu Photonics, Shizuoka, Japan) (Figure 3B). Computerized segmentation was performed using HALO 2022 (Indica Labs, Albuquerque, New Mexico, USA) using artificial intelligence. Several Dense Convolutional Networks (DenseNet) were trained with annotations reviewed by a pathologist (D.C.) [21]. The final AI analysis was evaluated on a slide-by-slide level by the pathologist and corresponded with his evaluation.

The first DenseNet differentiated between necrosis and viable tissue. Necrotic areas with negative staining were excluded. The second DenseNet segmented blood vessels and pools (Figure 3C). A blood pool is a cavity with red blood cells and <50% surrounding endothelial cells, whereas a blood vessel has $\geq 50\%$ endothelial cells. The blood vessel area (mm^2) and the number of blood vessels were counted and divided by the viable tissue area parameters to calculate the blood vessel area fraction (BVarea, %, Eq. 5) and the microvessel density (MVD) (Eq. 6).

$$\text{BVarea} = \frac{\text{blood vessel area } (\text{mm}^2)}{\text{viable tissue area}} \cdot 100 \quad (\text{BVarea} = \text{blood vessel area fraction}) \quad (5)$$

$$\text{MVD} = \frac{\text{number of blood vessels}}{\text{viable tissue area}} \quad (\text{MVD} = \text{microvessel density}) \quad (6)$$

Furthermore, a third and a fourth DenseNet were trained for calculating the number of GCs and NCs (Figure 3 D/E). Those were divided by the viable tissue area as well (Eqs. 7 and 8).

$$\text{GC}/\text{mm}^2 = \frac{\text{number of giant cells}}{\text{mm}^2 \text{ viable tissue}} \quad (\text{GC} = \text{giant cell}) \quad (7)$$

$$\text{NC}/\text{mm}^2 = \frac{\text{number of neoplastic cells}}{\text{mm}^2 \text{ viable tissue}} \quad (\text{NC} = \text{neoplastic cell}) \quad (8)$$

A semi-quantitative evaluation was made by a pathologist (D.C.) to evaluate the blood-pool-area-fraction of all slides from one tumor and the woven bone area fraction in the treated tumor (new bone formed by osteoblasts). An example of a typical area of woven bone is illustrated in Figure 3F.

Statistical analysis

CT and/or (DCE-)MRI were available shortly before or after curettage or biopsy to assess correlation between pathology and (DCE-)MRI parameters. Statistical analysis

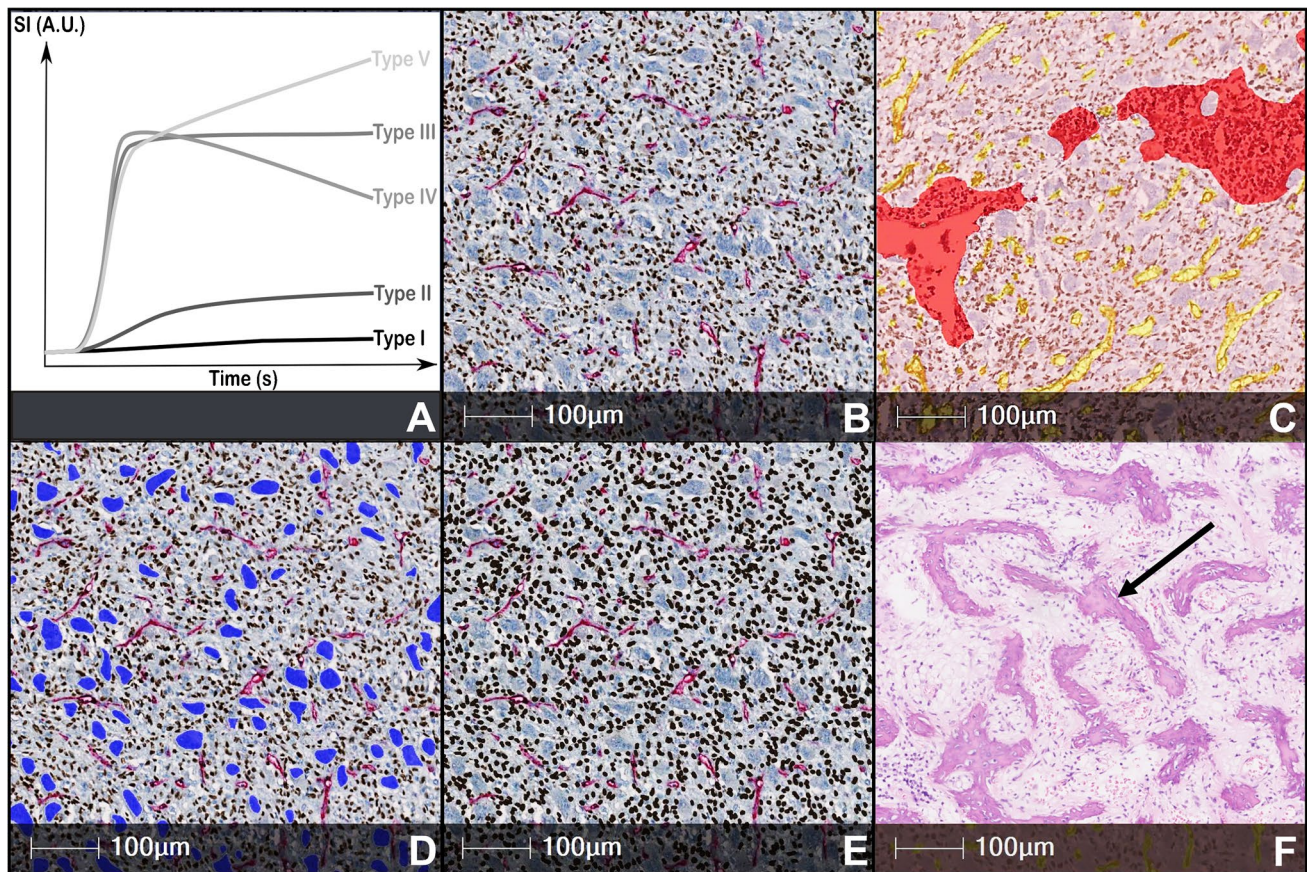


Fig. 3 Radiological and histopathological evaluation. **A** The radiological evaluation of the dynamic contrast-enhanced MRI time-intensity curve. Five types of time-intensity curves in qualitative analysis of giant cell tumors of bone with dynamic contrast-enhanced MRI can be distinguished. Type I has very low or no enhancement. Type II has slow sustained enhancement. Types III/IV/V curves have a steep wash-in and first pass (high perfusion, high tissue vascularization, low capillary resistance, high capillary permeability). Type III has a plateau in second phase. Type IV has a rapid wash-out in second phase (small interstitial space, high cellularity). Type V has a continuous wash-in (large interstitial space) in the second phase. **B–F** The histopathological evaluation. **B** An original stained microscopic slide without postprocessing to segment certain regions-of-interest. Red endothelial cells are stained with CD34 and represent blood

vessels. Brown cells are stained with H3.3G34W and represent neoplastic cells. **C** A microscopic slide (CD34 and H3.3G34W double-stained) with an overlay of the DenseNet automatic segmentation with HALO 2022 (Indica Labs, Albuquerque, New Mexico, USA) of blood vessels in yellow, background in pink, and blood pools in red. **D** A microscopic slide (CD34 and H3.3G34W double-stained) with an overlay of the DenseNet automatic segmentation with HALO 2022 (Indica Labs, Albuquerque, New Mexico, USA) with giant cells in blue. **E** A microscopic slide (CD34 and H3.3G34W double-stained) with an overlay of the DenseNet automatic segmentation with HALO 2022 (Indica Labs, Albuquerque, New Mexico, USA) with neoplastic cells in brown. **F** A slide stained with hematoxylin and eosin and is an example of a typical area of woven bone (black arrow). *A.U.* = arbitrary unit; *s* = second; *SI* = signal intensity; μm = micrometer

was performed with SPSS Statistics 28 (IBM, Armonk, New York, USA). Non-parametric tests were used because of the small sample size. The Pearson's correlation and Spearman's rank coefficient were calculated. In addition, the Kruskal-Wallis test by ranks was calculated to compare the distribution of pathology parameters across groups with a different TIC type. The significance level was set at $p < 0.05$ for all statistical tests.

Because all patients that were not treated with denosumab underwent initial tumoral resection, no control group was included.

Results

Patient characteristics

Because one sample was negative for H3.3G34W staining, which is highly sensitive (91–93%) and specific (99%) for the diagnosis of GCTB [22, 23], the decision was made to exclude this case from further statistical analysis (Figure 2).

A total of six patients (mean 28 ± 8 years; five males) were included in this proof-of-concept study. Patient characteristics are displayed in Table 1. Two patients underwent

curettage, 9 and 10 months after stopping denosumab because of recurrence (Table 1, patients 3 and 4) and two patients had a curettage 4 and 5 months after stopping denosumab (Table 1, patients 1 and 2), without recurrence of GCTB. One patient had a dental problem after a tooth extraction with a difficult and prolonged wound recovery, and one patient discontinued denosumab therapy because of a pregnancy wish. Both situations are known to be at risk of complications. Two patients did not stop denosumab treatment, so they did not have a curettage after denosumab treatment (Table 1, patients 5 and 6). The mean follow-up time was 6 ± 3 years (range 2–9).

Correlation of DCE-MRI with histopathology

No correlations were found using the tumoral DCE-MRI parameters relative to arterial enhancement. The parameters relative to muscle were more representative so only those were described.

Statistically significant linear correlations were found between MVD and TTP ($r = -0.8$; $p = 0.02$), between MVD and K_{trans} ($r = 0.8$; $p = 0.04$), between blood-pool-area-fraction and K_{trans} ($r = -0.9$; $p = 0.01$) and between blood-pool-area-fraction and area-under-the-time-concentration curve ($r = -0.8$; $p = 0.04$). Moreover, more statistically significant correlations were found with the Spearman's test. Strongest correlations were the correlation of MVD with TTP ($\rho = -0.9$; $p = 0.01$), MVD with the efflux rate constant (K_{ep}) ($\rho = 0.9$; $p = 0.01$), MVD with positive enhancement integral ($\rho = 0.9$; $p = 0.01$), and blood-pool-area-fraction with area-under-the-time-concentration curve ($\rho = -0.9$; $p = 0.01$). Overall, the blood vessel area fraction and MVD showed correlations with the same DCE-MRI parameters,

but MVD had more and stronger statistically significant correlation coefficients (Table 2).

Cases with a type IV TIC contained most NCs, GCs, and blood vessels. Cases with type V TIC had less NC, GC, and blood vessels, and cases with type II TIC had the least NCs, GCs, and blood vessels. Table 3 shows the mean, the standard deviation, and the range of NCs, GCs, and MVD of GCTBs with TIC curve types II, IV, and V. Moreover, a GCTB with TIC type II had statistically significant less NCs ($p = 0.03$) and GCs ($p = 0.04$) than a GCTB with TIC type IV (Figure 4).

Effects of denosumab on imaging and pathology with correlation

On CT, a tumor volume decrease was observed (mean $-0.05 \text{ cm}^3/\text{month}$); however, the volume before and after denosumab treatment was not significantly different. An HU increase (re-ossification, mean $+7.8 \text{ HU/month}$) was observed after denosumab treatment, which correlates microscopically with woven bone from the two patients undergoing curettage 4–5 months after stopping denosumab. On average, the woven bone area fraction of the microscopic slides was 80%. However, a re-occurrence of an HU decrease (new osteolysis) in the two patients undergoing curettage 9–10 months after therapy stop was observed. Microscopically, this was associated with only a few woven bone spots (5% of the slides) (Figure 5).

On MRI, all patients under denosumab treatment showed an SI decrease relative to muscle on T1w and T2FSw sequences with an average of -0.01 and -0.03 A.U./month , respectively. This correlates with woven bone formation on pathology. When denosumab was discontinued, the SI relative to muscle of T1w and T2FSw sequences increased

Table 1 Demographics of the included patients

Patient	Location	H3.3G34W staining	Age at diagnosis (years)	M/F	Reason stopping denosumab	Time to curettage after stopping denosumab (months)
1	Distal radius	Positive	36	M	Patient choice	4
2	Distal ulna	Positive	20	M	Neoadjuvant therapy	5
3	Pelvis	Positive	35	F	Pregnancy	9
4	Distal femur	Positive	35	M	Dental problem	10
5	Proximal tibia	Positive	20	M	/	/
6	Proximal femur	Positive	30	M	/	/
7	Proximal humerus	Negative	18	M	/	/
			$\mu = 27.7$ years			
			$\sigma = 8.1$ years			

Patients 1 and 2 had a curettage early after stopping denosumab (4–5-month time interval), while patients 3 and 4 had a curettage late after stopping denosumab (9–10-month time interval). In patients 5, 6, and 7, denosumab was not stopped. Therefore, there was no curettage after denosumab treatment for these patients

μ = mean; σ = standard deviation; F = female; M = male

Table 2 Pearson's correlation coefficients and Spearman's rank correlations of statistically significant correlations between MRI parameters and pathology parameters on all included patients

Correlations	PCC	<i>p</i> -value	SRC	<i>p</i> -value
MVD - TTP	-0.8	0.02	-0.9	0.01
MVD - WI	/	/	0.8	0.04
MVD - AUC TIC	/	/	0.8	0.04
MVD - PEI	/	/	0.9	0.01
MVD - <i>K</i> trans	0.8	0.04	0.8	0.04
MVD - <i>K</i> ep	/	/	0.9	0.01
MVD - AUC TCC	/	/	0.8	0.02
BVArea - TTP	/	/	-0.8	0.04
BVArea - <i>K</i> ep	/	/	0.8	0.04
BPArea - <i>K</i> trans	-0.9	0.01	-0.9	0.01
BPArea - AUC TCC	-0.8	0.04	-0.9	0.01

AUC TCC area-under-the-time-concentration curve; *AUC TIC* area-under-the-time-intensity-curve; *BPArea* blood pool area fraction; *BVArea* blood vessel area fraction; *Kep* efflux rate constant; *Ktrans* volume transfer constant; *MVD* microvessel density; *PCC* Pearson's correlation coefficient; *PEI* positive enhancement integral; *SRC* Spearman's rank correlation coefficient; *TTP* time-to-peak; *WI* wash-in

Table 3 Descriptive statistics of the number of neoplastic cells (NC/mm²), giant cells (GC/mm²), and the microvessel density across giant cell tumors of bone with a different time-intensity curve

TIC	NC/mm ²	GC/mm ²	MVD
Type IV			
Mean	4150	116	148
Standard deviation	617	55	90
Range	3400-4774	16-140	84-325
Type V			
Mean	2403	41	122
Standard deviation	808	28	39
Range	1472-3408	5-69	68-160
Type II			
Mean	789	14	122
Standard deviation	757	19	70
Range	254-1324	1-28	72-171

Giant cell tumors of bone with a time-intensity curve type IV had the most neoplastic cells, giant cells, and blood vessels, followed by giant cell tumor of bone type V. In addition, giant cell tumors of bone type II had statistically significant less neoplastic cells ($p = 0.03$) and giant cells ($p = 0.04$) compared to type IV

GC giant cell; *MVD* microvessel density; *NC* neoplastic cell; *TIC* time-intensity curve

again, even faster than the decrease under treatment (+0.05 and +0.09 A.U./month, respectively). This is indicative of disappearance of woven bone and increasing tumoral infiltration. Only a few spots of woven bone on pathology in those two patients were identified (5% of the slide).

When analyzing the DCE-MRI, initially all patients receiving treatment with denosumab had a TIC shift from type IV to II (and to type V in one patient), an area-under-the-time-intensity-curve (mean -72%) and *K*trans (mean -71%) decrease and TTP (mean +100%) increase. The second phase of TIC changed as well from a negative to a positive wash-out slope indicating continuous wash-in instead of a rapid wash-in and wash-out phenomenon, which is characteristic for a decrease in blood vessels and a larger extracellular volume to distribute the gadolinium contrast agent inflow. All parameters but wash-out slope and the extracellular-extravascular-volume-fraction showed significant changes (Table 4). These findings corresponded with pathology, where patients treated with denosumab had a decrease in MVD (mean -28%), in GC/mm² (mean -76%), and in NC/mm² (mean -63%). All patients treated with denosumab also showed an increase in blood pools (mean +84%).

When stopping denosumab, TIC shifted to a type IV curve again indicating a relapse. Table 5 and Figure 6 show the differences in (DCE-)MRI parameters and in pathology parameters of the two patients who had a curettage early after stopping denosumab (4–5 months), compared to the two patients who had a late curettage after stopping denosumab (9–10 months). Patients with early curettage showed a decrease in T1w and in T2FSw SI, compared to an increase in SI in patients with a late curettage. Patients with a late curettage show a lower decrease in wash-in slope, area-under-the-time-intensity-curve, *K*trans, area-under-the-time-concentration-curve, MVD, GCs, and NCs and a lower increase in TTP and blood-pool-area-fraction after denosumab treatment compared to patients with early curettage, indicating recurrence.

Correlation of vascularization and aggressiveness

A statistically significant association was observed between MVD and cortical breakthrough. All patients with an MVD higher than 130 vessels/mm² (three patients) had cortical breakthrough as observed on CT/MRI imaging. No correlation was found with the blood vessel area fraction or tumor size.

Discussion

A strong linear correlation was found between MVD and *K*trans, while a strong linear inverse correlation was found between MVD and TTP. A higher density of blood vessels allows faster inflow of gadolinium contrast agent into the GCTB, increasing the *K*trans and shortening the TTP. Between MVD and wash-in slope, only a significant rank correlation coefficient was found, which suggests that wash-in slope is, apart from the MVD, more influenced

Fig. 4 Boxplot-and-whisker plots of the number of neoplastic cells/mm², the number of giant cells/mm², and the microvessel density observed in giant cell tumors of bone with time-intensity curve type IV (left column), curve type V (middle column), and curve type II (right column). The boxes represent the Q1-Q3 interquartile range (IQR). The horizontal line in the boxes represents the median value. The lower boundary of the lowest whisker represents Q1-1.5*IQR. The upper boundary of the highest whisker represents Q3+1.5*IQR. Diamonds represent low and high extreme outliers below Q1-3.0*IQR or above Q3+3.0*IQR. *GC* = giant cells; *MVD* = microvessel density; *NC* = neoplastic cells; *SI* = signal intensity; *TIC* = time-intensity curve

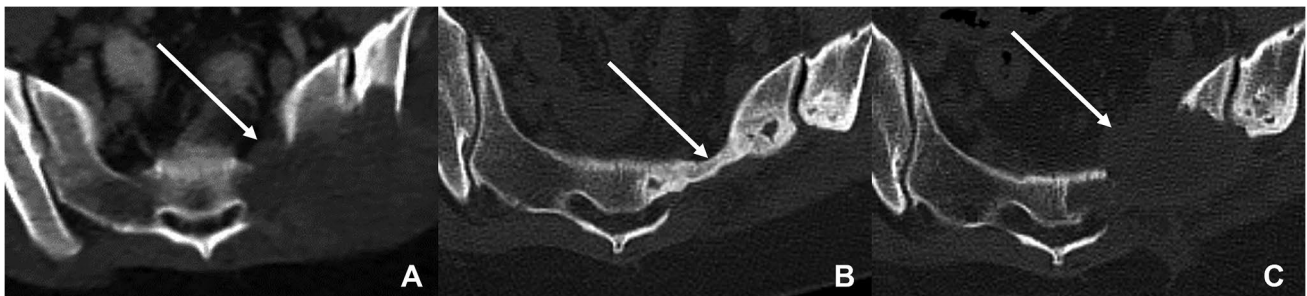
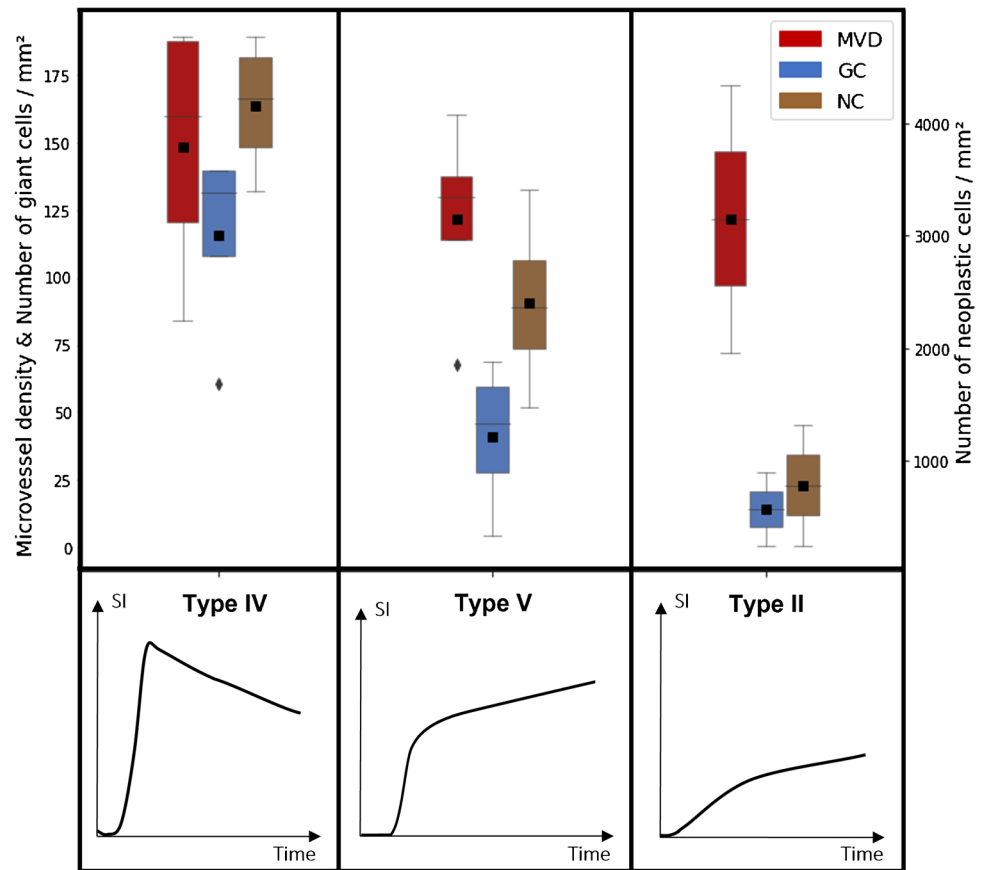


Fig. 5 CT follow-up of a 35-year-old female patient with a giant cell tumor of bone expanding in the sacrum, left iliac bone, and surrounding soft tissues. **A** The GCTB before denosumab treatment, showing an osteolytic lesion in the left hemi-sacrum (white arrow) expanding in the left iliac bone and in the surrounding soft tissues. Complete destruction of the posterior aspect of both the sacrum and iliac bone is observed. **B** The same lesion after 2.5 years of denosumab treatment. A re-ossification of the tumor is seen with an increase lesion

density (white arrow). **C** Nine months after stopping denosumab treatment because of a pregnancy wish, a re-occurrence of the GCTB is observed as a new osteolytic lesion at the exact same location as the original tumor (white arrow). In comparison to the GCTB at diagnosis, both the anterior and posterior cortical borders of the left hemi-sacrum and left iliac bone are completely destroyed with both anterior and posterior extension of the GCTB into the soft tissues

by other parameters that were not assessed (e.g., capillary permeability). No correlation was found with the extracellular-extravascular-volume-fraction (V_e), probably because it is strongly influenced by the viscosity/bulk water flow of the extracellular space, which was not assessed. Additionally, a linear inverse correlation was found between the blood-pool-area-fraction and the K_{trans} . K_{trans} reflects the

combined effects of plasma blood flow and blood vessel permeability. Blood pools are large cavities, which are not delineated by endothelial cells, filled with red blood cells. In such large cavities, the bulk water flow approaches zero, explaining why the K_{trans} decreases with increased blood pools. The area-under-the-time-concentration-curve was inversely correlated with blood-pool-area-fraction, which

Table 4 Descriptive statistics, change of size, and contrast enhancement parameters before and after denosumab treatment and statistical difference evaluation (*p*-value of Wilcoxon signed-rank test)

Parameter	Before denosumab Mean ± SD	After denosumab Mean ± SD	Absolute change (%)	<i>p</i> -value
Volume (cm ³)	196 ± 171	195 ± 172	−2 (−1%)	0.21
WI*	20 ± 15	4 ± 4	−16 (−80%)	0.04
WO*	−6 ± 6	6 ± 7	+12 (+203%)	0.08
TTP*	0.5 ± 0.1	1 ± 0.1	+0.5 (+100%)	0.04
PEI*	7 ± 5	2 ± 1	−5 (−70%)	0.04
AUC TIC*	12 ± 9	3 ± 3	−8 (−72%)	0.04
<i>K</i> trans*	15 ± 6	4 ± 4	−11 (−71%)	0.04
<i>K</i> ep*	4 ± 2	1 ± 1	−3 (−71%)	0.04
<i>V</i> e*	2 ± 4	3 ± 2	+0.6 (+29%)	0.14
AUC TCC*	12 ± 5	4 ± 4	−9 (−71%)	0.04
TIC type	IV	II	IV → II	/

WO, TTP, and *V*e increased after receiving denosumab treatment. All other parameters decreased. All parameters but volume, WO, and *V*e showed significant changes

AUC TCC area-under-the-time-concentration curve; AUC TIC area under-the-time-intensity curve; *K*ep efflux rate constant; *K*trans volume transfer constant; PEI positive enhancement integral; SD standard deviation; TIC time-intensity-curve; TTP time-to-peak; *V*e extracellular-extravascular-volume-fraction; WI wash-in; WO wash-out

*All values are relative values to a reference muscle

Table 5 Comparison of (DCE-) MRI parameters and pathology parameters pre-denosumab and post-denosumab in patients with an early curettage after stopping denosumab (4–5 months) and patients with late curettage after stopping denosumab (9–10 months)

Parameter	Mean change of parameters (%) pre-denosumab vs. early curettage post-denosumab	Mean change of parameters (%) pre-denosumab vs. late curettage post-denosumab
T1 SI	−8	+11
T2FS SI	−9	+11
TIC type	Type IV → type II	Type IV = type IV
WI	−81	−68
TTP	+92	+55
AUC TIC	−60	−53
<i>K</i> trans	−70	−45
AUC TCC	−68	−57
GC/mm ²	−97	−55
NC/mm ²	−77	−49
MVD	−32	−23
BPArea	+117	+50

Patients with a late curettage after stopping denosumab showed less effect of denosumab treatment, indicating a relapse. The most prominent differences on histopathology were seen in the blood pool area fraction (BPArea) and in the giant cells (GC) per mm² and on DCE-MRI in time-to peak (TTP)

AUC TCC area-under-the-time-concentration-curve; AUC TIC area-under-the-time-intensity-curve; BPArea blood pool area fraction; GC giant cells; *K*trans volume transfer constant; MVD microvessel density; NC neoplastic cells; SI signal intensity; TIC time-intensity curve; TTP time-to-peak; T1 T1-weighted images; T2FS fat-saturated T2-weighted images; vs versus; WI wash-in

is also regulated by the blood flow. The GCs and the NCs correlated with the TIC type: A TIC type IV had significantly more GCs and NCs compared to a type II.

The effect of denosumab treatment was pathologically more pronounced on the GCs than on the NCs. This can be explained by denosumab having a direct effect on the GCs by preventing the RANKL to bind to the RANK. Some NCs will always

survive between the newly formed woven bone trabeculae. This can be the reason why patients relapsed after discontinuing denosumab treatment, as described in previous studies and in our study population [1, 5, 6, 8]. Following our data, recurrence is most likely to occur around 9–10 months after discontinuing treatment. Even after curettage, NCs tend to survive in the margins of the tumor, with a high risk of recurrence.

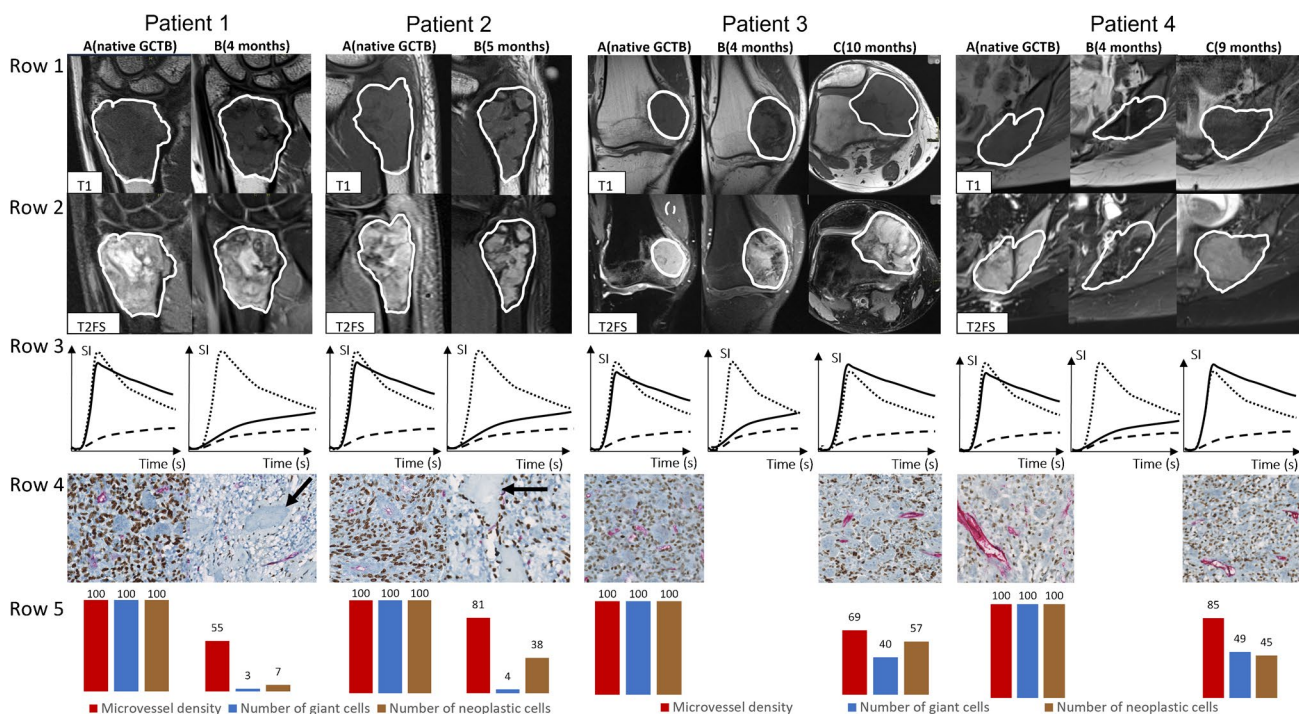


Fig. 6 The effect of denosumab on giant cell tumors of bone in four patients. In each of these patients, two or three columns can be observed (A, B, C). Column **A** represents the native giant cell tumor of bone at diagnosis and before denosumab treatment. Column **B** represents the giant cell tumor of bone 4 months (patients 1, 3, 4) to 5 months (patient 2) after stopping denosumab treatment. Column **C** represents the giant cell tumor of bone nine (patient 4) to 10 months (patient 3) after stopping denosumab treatment. Row one shows T1-weighted images. Row two shows fat-saturated T2-weighted images. Row three displays the time-intensity curve of the giant cell tumor of bone compared to the artery and muscle as reference tissues (tumor = solid line, muscle = dashed line, artery = dotted line). Row four represents the microscopic slides ($\times 20$). Red cells are stained with CD34, representing endothelial cell lining blood vessels. Brown cells are stained with H3.3G34W, representing neoplastic cells. Row five represents the change in % of the number of blood vessels (microvessel density), giant cells, and neoplastic cells, where the microvessel density, number of giant cells, and number of neoplastic cells in the native giant cell tumor of bone at diagnosis are set to 100% before start of denosumab therapy. In patients 1 and 2, the native tumors (column A) have a relatively low signal intensity on T1-weighted images, a high signal intensity on fat-saturated T2-weighted images, and a time-intensity curve type IV. This corresponds with a highly cellular environment with an abundance of blood vessels, a small extracellular space, and large amounts of

giant cells and neoplastic cells (rows 4 and 5). Both patients show a good response to denosumab therapy (column B) after 4–5 months with a decrease of signal intensity on T1-weighted and on fat-saturated T2-weighted images due to re-ossification. The time-intensity curve of both patients (row 3) changed from type IV to type II due to a decrease in number and permeability of blood vessels and an increase in extracellular space as observed on the microscopic slides. Furthermore, woven bone is observed (black arrows, row 4) with foamy macrophages and a decrease in the number of giant cells and neoplastic cells. In patients 3 and 4, initially a good response to denosumab treatment is observed after 4 months (column B), with a decrease of signal intensity on T1-weighted images and fat-saturated T2-weighted images and a shift of time-intensity curve from type IV to II. However, 9–10 months after stopping denosumab (column C), signal intensity on T1-weighted and fat-saturated T2-weighted images starts to increase again. Tumoral time-intensity curve evolves to a type IV curve (row 3) again. This correlates with the relative increase of number of giant cells and neoplastic cells and maintained high microvessel density (rows 4 and 5) as compared to the patients with sustained good response (patients 1 and 2). On microscopic examination, a relapse with a more cellular environment is observed with disappearance of the woven bone, a new increase of blood vessels, and increased giant cells and neoplastic cells. *GCTB* = giant cell tumor of bone; *SI* = signal intensity; *T1* = T1-weighted images; *T2FS* = T2-weighted images with fat saturation

Susarla et al. stated that GCTB of the jaw, with a blood vessel area fraction of $>2.5\%$, was significantly more aggressive. In their classification system, they analyzed the largest tumoral diameter and cortical breakthrough. In this study, no significant association with the blood vessel area fraction was observed. However, there was a significant correlation between MVD and cortical breakthrough

[13]. This supports their conclusion that vascularization of GCTB is associated with aggressiveness. Min et al. stated that vascular endothelial growth factor induces RANK expression by endothelial cells, making them more responsive to RANKL effects. Moreover, RANKL stimulates the survival of endothelial cells, promotes neo-angiogenesis, and increases vascular permeability, independently from

vascular endothelial growth factor activity. This theory could explain the association between high vascularization and aggressiveness [14–16]. This would also explain why MVD decreases under denosumab treatment. As denosumab binds to RANKL, less RANKL would be available to stimulate the survival of endothelial cells. Additionally, the vascular permeability would decrease under denosumab.

This article is a proof-of-concept study on the correlation between imaging assessment and histology on six patients. All patients were used for evaluation of correlation between pathology and DCE-MRI. Other groups have studied the effects of denosumab on pathology in larger patient groups. However, we study the effect of denosumab on vascularization, tumoral cells, tumoral microenvironment, bone formation, and imaging findings by correlating them to pathology. This proof-of-concept study shows a good correlation between pathology and radiology, especially between the MVD and TTP and between the curve type and the numbers of NCs and GCs. However, because of the small sample size, extrapolation of results to all patients should be done with some caution. Larger multicenter studies with a larger study population are needed in the future to confirm or fine-tune these findings.

A limitation of this small study is that pathology only samples a small part of a larger tumor. Because this is a retrospective study, no point-to-point correlation could be performed. Future studies should add a point-to-point correlation between different zones on both CT/MRI evaluation and histopathology to assess the true nature of different tumoral components. In conclusion, pathological response to denosumab shows a decrease of approximately 97% of GCs, accompanied by a decreased MVD of 32%. On DCE-MRI, this correlates with an increase of TTP by approximately 100% and a change of TIC from type IV to type II. As soon as denosumab is stopped, GCs start proliferating again and NCs are stimulated. This is accompanied with an increase in MVD, a decrease of approximately 37% in TTP, and the time TIC type changing again to type IV. On CT, a tumor volume decrease (mean $-0.05 \text{ cm}^3/\text{month}$) and an HU increase (re-ossification, mean $+7.78 \text{ HU/month}$) were observed. These results suggest that CT and DCE-MRI can help to guide diagnostic and follow-up decisions of GCTB. Larger international studies are needed to validate these results.

Acknowledgements We would like to thank for technical support Sukru Karanfil, Ran Rumes and Lynn Supply from the pathology department. We would also like to thank Louis Deconinck for his help with the data analysis.

Data availability Data generated or analyzed during the study are available upon reasonable request.

References

1. Chawla S, Blay J-Y, Rutkowski P, Le Cesne A, Reichardt P, Gelderblom H, et al. Denosumab in patients with giant-cell tumour of bone: a multicentre, open-label, phase 2 study. *Lancet Oncol.* 2019;20(12):1719–29.
2. WHO Classification of Tumours Editorial Board. *Soft Tissue and Bone Tumours: WHO Classification of Tumours (Medicine)*. 5th ed. International Agency for Research on Cancer; 2020.
3. Santini E, Kalil RK, Franco Bertoni Y-KP. Tumors and tumorlike lesions of bone, vol. 25. Springer; 1994. p. 593–3.
4. Presneau N, Baumhoer D, Behjati S, Pillay N, Tarpey P, Campbell PJ, et al. Diagnostic value of H3F3A mutations in giant cell tumour of bone compared to osteoclast-rich mimics. *J Pathol Clin Res [Internet]*. 2015;1(2):113–23. <https://doi.org/10.1002/cjp2.13>.
5. Zhang R, Ma T, Qi D, Zhao M, Hu T, Zhang G. Short-term preoperative denosumab with surgery in unresectable or recurrent giant cell tumor of bone. *Orthop Surg.* 2019;11(6):1101–8.
6. Lipplaa A, Dijkstra S, Gelderblom H. Challenges of denosumab in giant cell tumor of bone, and other giant cell-rich tumors of bone. *Curr Opin Oncol.* 2019;31(4):329–35.
7. van der Heijden L, Dijkstra PDS, Blay J-Y, Gelderblom H. Giant cell tumour of bone in the denosumab era. *Eur J Cancer.* 2017;77:75–83.
8. Mak IWY, Evaniew N, Popovic S, Tozer R, Ghert M. A translational study of the neoplastic cells of giant cell tumor of bone following neoadjuvant denosumab. *J Bone Joint Surg Am.* 2014;96(15):e127.
9. Thomas D, Henshaw R, Skubitz K, Chawla S, Staddon A, Blay J-Y, et al. Denosumab in patients with giant-cell tumour of bone: an open-label, phase 2 study. *Lancet Oncol.* 2010;11(3):275–80.
10. Chawla S, Henshaw R, Seeger L, Choy E, Blay J-Y, Ferrari S, et al. Safety and efficacy of denosumab for adults and skeletally mature adolescents with giant cell tumour of bone: interim analysis of an open-label, parallel-group, phase 2 study. *Lancet Oncol.* 2013;14(9):901–8.
11. Gossai N, Hilgers MV, Polgreen LE, Greengard EG. Critical hypercalcemia following discontinuation of denosumab therapy for metastatic giant cell tumor of bone. *Pediatr Blood Cancer.* 2015;62(6):1078–80.
12. van Langevelde K, McCarthy CL. Radiological findings of denosumab treatment for giant cell tumours of bone. *Skeletal Radiol.* 2020;49(9):1345–58.
13. Susarla SM, August M, Dewsnup N, Faquin WC, Kaban LB, Dodson TB. CD34 staining density predicts giant cell tumor clinical behavior. *J Oral Maxillofac Surg.* 2009;67(5):951–6.
14. Girolami I, Mancini I, Simoni A, Baldi GG, Simi L, Campanacci D, et al. Denosumab treated giant cell tumour of bone: a morphological, immunohistochemical and molecular analysis of a series. *J Clin Pathol.* 2016;69(3):240–7.
15. Yang Y-Q, Tan Y-Y, Wong R, Wenden A, Zhang L-K, Rabie ABM. The role of vascular endothelial growth factor in ossification. *Int J Oral Sci.* 2012;4(2):64–8.
16. Min J-K, Cho Y-L, Choi J-H, Kim Y, Kim JH, Yu YS, et al. Receptor activator of nuclear factor (NF)-kappaB ligand (RANKL) increases vascular permeability: impaired permeability and angiogenesis in eNOS-deficient mice. *Blood.* 2007;109(4):1495–502.
17. van der Woude HJ, Verstraete KL, Hogendoorn PC, Taminiou AH, Hermans J, Bloem JL. Musculoskeletal tumors: does fast dynamic contrast-enhanced subtraction MR imaging contribute to the characterization? *Radiology.* 1998;208(3):821–8.
18. Lavini C, de Jonge MC, van de Sande MGH, Tak PP, Nederveen AJ, Maas M. Pixel-by-pixel analysis of DCE MRI curve patterns

- and an illustration of its application to the imaging of the musculoskeletal system. *Magn Reson Imaging*. 2007;25(5):604–12.
19. Van Den Berghe T, Verstraete KL, Lecouvet FE, Lejoly M, Dutoit J. Review of diffusion-weighted imaging and dynamic contrast-enhanced MRI for multiple myeloma and its precursors (monoclonal gammopathy of undetermined significance and smouldering myeloma). *Skeletal Radiol*. 2022;51(1):101–22.
 20. Cuenod CA, Balvay D. Perfusion and vascular permeability: basic concepts and measurement in DCE-CT and DCE-MRI. *Diagn Interv Imaging* [Internet]. 2013;94(12):1187–204. <https://doi.org/10.1016/j.diii.2013.10.010>.
 21. Huang G, Liu Z, Van Der Maaten L, Weinberger KQ. Densely connected convolutional networks. In: 2017 IEEE Conference on Computer Vision and Pattern Recognition (CVPR); 2017. p. 2261–9.
 22. Amary F, Berisha F, Ye H, Gupta M, Gutteridge A, Baumhoer D, et al. H3F3A (Histone 3.3) G34W immunohistochemistry: a reliable marker defining benign and malignant giant cell tumor of bone. *Am J Surg Pathol*. 2017;41(8):1059–68.
 23. Yang L, Zhang H, Zhang X, Tang Y, Wu Z, Wang Y, et al. Clinico-pathologic and molecular features of denosumab-treated giant cell tumour of bone (GCTB): analysis of 21 cases. *Ann Diagn Pathol* [Internet]. 2022;57:151882. <https://www.sciencedirect.com/science/article/pii/S1092913421001829>

Publisher's note Springer Nature remains neutral with regard to jurisdictional claims in published maps and institutional affiliations.

Springer Nature or its licensor (e.g. a society or other partner) holds exclusive rights to this article under a publishing agreement with the author(s) or other rightsholder(s); author self-archiving of the accepted manuscript version of this article is solely governed by the terms of such publishing agreement and applicable law.